CHEMISTRY OF MATERIALS

Article

pubs.acs.org/cm

Aerosol-Assisted Synthesis of Shape-Controlled $CoFe_2O_4$: Topotactic versus Direct Melt Crystallization

Jie Fu, Christopher J. DeSantis,† Rebecca G. Weiner, and Sara E. Skrabalak*

Department of Chemistry, Indiana University, Bloomington, Indiana 47405, United States

Supporting Information

ABSTRACT: Compositionally complex materials can be prepared as nanocrystals with defined shapes by aerosol-assisted molten salt synthesis (AMSS), where the aerosol phase spatially and temporally confines crystal growth. Here, single-crystalline $CoFe_2O_4$ nanoplates and $CoFe_2O_4$ octahedra are achieved selectively by AMSS through the use of Na_2CO_3 and Na_2MoO_4 fluxes, respectively. The formation of $CoFe_2O_4$ nanoplates is generally unexpected given the cubic crystal symmetry of spinel ferrites, but this shape is accounted for by in situ formation of a layered double hydroxide (LDH) intermediate stabilized by the CO_3^{2-} anions of the flux. Topotactic conversion of the LDH intermediate to $CoFe_2O_4$ preserves the plate morphology of the LDH crystals. In contrast, the formation of the LDH intermediate is not possible with the Na_2MoO_4 flux. Thus, product formation proceeds via crystallization from the molten media, with octahedral crystals consistent with the common crystal habit of the spinel phase produced. This demonstration of topotactic chemistry within the aerosol phase is significant given the range of LDH phases available for conversion to mixed metal oxides, where the AMSS technique facilitates shape-controlled nanocrystal formation.

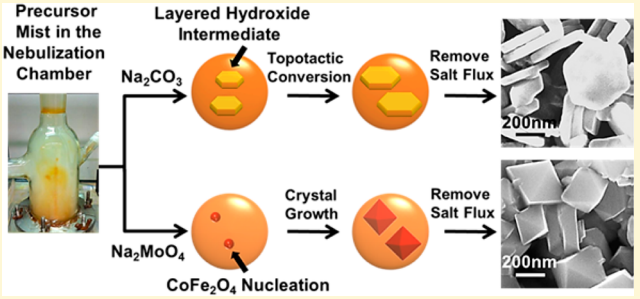

INTRODUCTION

The properties of materials depend on crystallite size, shape, composition, and architecture, with considerable efforts being directed toward the synthesis of structurally defined nanocrystals.[1−4] Ultrasonic spray synthesis (USS) is a simple, generalizable way to continuously produce materials of many classes, including complex metal oxides.[5,6] First, aerosol droplets are generated from an ultrasonic source and transported into a heated zone. There, solvent evaporation, precipitation, or reaction of precursors occur, and powders comprised of polycrystalline microspheres are commonly produced.[7,8] This particle structure arises as numerous nuclei typically exist within a droplet and traditional aerosol chemistry is insufficient to inhibit agglomeration of these crystallites. Recently, molten salt syntheses have been coupled with USS to produce single-crystalline nanoparticles, often with shape control.[9−11] The formation of nanocrystals is enabled by the salt media inhibiting aggregation of the individual crystallites, while the spatial and temporal confinement of the aerosol phase limits crystal growth to the nanoscale. Aerosol-assisted molten salt synthesis (AMSS) typically involves a crystallization process, where nucleation and growth of product is initiated by loss of volatile species from or cooling of aerosol droplets.[11] The presence of a molten phase in AMSS often results in faceted crystals of equilibrium form that are commonly observed in nature.[12] Although AMSS is an effective way to control the shape of nanocrystals of compositionally complex materials, the factors that dictate structure control are poorly understood. Additionally, strategies are needed for AMSS to produce materials with new crystal shapes. With $CoFe_2O_4$ as a model system, shape-control is demonstrated here through flux selection, with nanoplates and octahedra selectively achieved. These different morphologies are accounted for by whether the selected flux facilitates formation of a layered double hydroxide (LDH) intermediate prior to product formation.

Spinel ferrites such as $CoFe_2O_4$ are promising materials for magnetic,[13,14] electrochemical,[15] and photocatalytic applications.[16] They have been synthesized by thermal decomposition of organometallic precursors,[13] coprecipitation[14,17] as well as molten salt[18] and sol−gel methods.[19] In nature, minerals of the spinel family often adopt octahedral crystal habits,[20] and micrometer-sized octahedral $CoFe_2O_4$ particles have been obtained in a traditional MSS from presynthesized $CoFe_2O_4$ seeds.[18] Thus, $CoFe_2O_4$ octahedral crystals or related shapes would be anticipated from AMSS. However, in our previous study of γ-Fe_2O_3, which has a spinel crystal structure, nanoparticles with a plate-like morphology were produced by AMSS.[11] The formation of nanoplates is generally unexpected in these systems given the face-centered-cubic (fcc) symmetry of the crystals; however, topotactic transformation in which product preserves the shape of the precursor could generate crystals with morphologies that are far from the equilibrium crystal habit; for instance, spinel platelets can topotactically convert from LDH precursors.[21]

Received: January 11, 2015
Published: February 28, 2015

DOI: 10.1021/acs.chemmater.5b00109
Chem. Mater. 2015, 27, 1863−1868

LDHs consist of positively charged layers of metal−oxygen edge-sharing octahedra and weakly bound, charge-compensating anion (e.g., CO_3^{2-}, NO_3^-) interlayers. They are typically prepared from coprecipitation of metal hydroxides under alkaline condition, followed by aging of the solution.[17,21] The flexibility of LDHs to accommodate a wide range of both divalent and trivalent metal cations makes them suitable precursors to spinel phases, although in most cases, oxide of the divalent metal accompanies the spinel product.[22,23] The generation of these metal oxide byproducts arise from excess divalent metal cations in the LDH precursor. Interestingly, Mallouk and co-workers reported the synthesis of spinel platelets with {111} facets expressed via topotactic conversion of LDH precursors with plate-like morphology.[21] Here, such topotactic conversion chemistry is integrated with AMSS through the in situ generation of a LDH intermediate and provides access to new nanocrystal shapes. $CoFe_2O_4$ was selected as a model system, and a number of common salts were integrated with USS. Significantly, when the selected flux provides an alkaline condition and anions capable of stabilizing an LDH intermediate, nanoplates are produced. Otherwise, octahedra are produced, consistent with the crystallization mechanism of AMSS.

EXPERIMENTAL SECTION

Materials. All chemicals were handled in air and used as received. $Fe_2(SO_4)_3{\cdot}mH_2O$, $CoSO_4{\cdot}7H_2O$, Na_2CO_3, Na_2MoO_4, NaOH, Na_2SO_4, NaCl, and $CoFe_2O_4$ were purchased from Sigma-Aldrich. Deionized water was used for all syntheses.

Apparatus for USS. A schematic is shown in Figure S1 and described fully in the Supporting Information (SI).

AMSS of Shape-Controlled $CoFe_2O_4$ Nanocrystals. Solution concentrations of $Fe_2(SO_4)_3{\cdot}mH_2O$, $CoSO_4{\cdot}7H_2O$, and salt for flux formation were fixed at 0.025, 0.025, and 0.25 M, respectively. The reagents were dissolved in 15 mL of water and then sonicated/vortexed for 2 min for full dissolution/dispersion. The salts evaluated included Na_2CO_3, Na_2MoO_4, NaCl, Na_2SO_4, and NaOH. A brown precipitate formed during solution preparation with Na_2CO_3, and the pH of the final solution was 10.4. A brownishorange precipitate formed during solution preparation with Na_2MoO_4, and the pH of the precursor solution was 6.2. When NaCl and Na_2SO_4 salts were used, a clear yellow precursor solution with pH 1.5 and a clear peach precursor solution with pH 2.7 were obtained, respectively. The use of NaOH resulted in a dark brown precipitate upon solution preparation, where the pH of the solution was measured to be 11.3. These solutions or slurries were used as precursors with USS without further modification. Products produced from the use of NaCl, Na_2SO_4, or NaOH are denoted as CoFe-NaCl, CoFe-Na_2SO_4, and CoFe-NaOH, respectively. All precursor solutions and slurries were sparged with air for 20 min before nebulization. The furnace temperature was kept at 900 °C with an air flow rate of 95 sccm in all syntheses. The product was collected in one gas-washing bubbler containing water. The product was separated by centrifugation, with two additional water washings before the samples were dried.

USS of $CoFe_2O_4$ Microspheres. Fifteen milliliters (15 mL) of precursor solution with pH 1.5 containing 0.025 M $Fe_2(SO_4)_3{\cdot}mH_2O$ and 0.025 M $CoSO_4{\cdot}7H_2O$ was prepared. The clear solution was sparged with air for 20 min before nebulization. The furnace temperature was 900 °C with an air flow rate of 95 sccm.

MSS of $CoFe_2O_4$ as Reference Materials. First, 0.375 mmol $Fe_2(SO_4)_3{\cdot}mH2O$, 0.375 mmol $CoSO_4{\cdot}7H_2O$, and 3.75 mmol salt (Na_2CO_3 or Na_2MoO_4) were mixed and ground with a mortar and pestle. Then, about one-third of the ground powder was placed in a Pt pan and heated at 900 °C under air atmosphere for 1.5 h, with a ramp rate of 60 °C/min.

Attempted Syntheses of CoFe-LDH by Coprecipitation. The precursor solutions for AMSS, as described above, were prepared. Specifically, 0.025 M $Fe_2(SO_4)_3{\cdot}mH_2O$, 0.025 M $CoSO_4{\cdot}7H_2O$, and 0.25 M salt (Na_2CO_3, NaOH, or Na_2MoO_4) were dissolve in 15 mL of water to form a slurry. Rather than being used with USS, the resulting slurries were then heated in an oil bath at 80 °C overnight. The products were collected by centrifugation and washed with water several times. The products are denoted as CoFe-salt-80; for instance, when Na_2MoO_4 was used, the product is named CoFe-Na_2MoO_4-80.

AMSS of $CoFe_2O_4$ Nanoplates from CoFe-Na_2CO_3-80. First, 0.375 mmol of CoFe-Na_2CO_3-80 with or without 3.75 mmol Na_2CO_3 was dispersed in 15 mL water. Then, the slurry was sonicated/vortexed for 2 min and sparged with house air for 20 min before nebulization. The temperature of the furnace for AMSS was 900 °C with an air flow rate of 95 sccm. The product was collected in one gas-washing water bubbler. The product was then isolated by centrifugation, with two additional water washings before the product was dried.

Product Characterization. Scanning electron microscopy (SEM) was done with a FEI Quanta 600 FEG operating at 30 kV. An Oxford Inca detector for energy dispersive X-ray spectroscopy (EDS) was interfaced to the instrument. Transmission electron microscopy (TEM) and selected area electron diffraction (SAED) were performed using a JEOL JEM 3200FS at an accelerating voltage of 300 kV. Powder X-ray diffraction (XRD) was conducted with the Panalytical Empyrean diffractometer using Cu Kα as the radiation source. Raman spectroscopy was done with an InVia Renishaw Raman Microscope diode at a laser excitation wavelength of 785 nm. The samples were cast onto glass slides. Spectra were acquired at a power of 3 mW with a 50× numerical aperture objective (NA = 0.4). Differential scanning calorimetry (DSC) was performed with a Q10 TA DSC instrument at a ramp rate of 6 °C/min. Hermetic aluminum pans with a pinhole were used to facilitate the exchange of gas in and out of the pan under an atmosphere of air. Thermal gravimetric analysis (TGA) was performed with a Q5000 IR TA TGA instrument with a ramp rate of 6 °C/min under an air atmosphere. Platinum pans were employed for sample containers. For both DSC and TGA, the AMSS precursor solutions were prepared as described and then vacuum-dried to remove water prior to analysis.

RESULTS AND DISCUSSION

AMSS of Shape-Controlled $CoFe_2O_4$ Nanocrystals via Topotactic Transition. Many salts can be selected for the MSS of $CoFe_2O_4$; however, the role of flux selection on morphology development is poorly understood. We hypothesized that in a typical AMSS to $CoFe_2O_4$, where product formation proceeds via crystallization from the molten media, equilibrium crystal shapes would be achieved (octahedra or closely related forms such as cubes or cuboctahedra). In contrast, the crystal shape could be modified by changing the pathway to product, in which the molten salt media would stabilize a LDH intermediate that could undergo thermal topotactic conversion to the spinel phase. This conversion process is represented by Figure 1, in which the rhombohedral structure ($R3m$) of the LDH along [001] is crystallographically related to the fcc structure ($Fd3m$) of the spinel along the [111]. The layered nature of LDHs drives these materials to adopt plate-like crystal habits in which the {001} facets are preferentially expressed. Topotactic conversion of the LDH phase will lead to the spinel with expression of {111} facets due to the correlated symmetry between LDH {001} sheets and spinel {111} facet. To generate a CoFe-based LDH intermediate during AMSS and ultimately $CoFe_2O_4$ nanoplates, Na_2CO_3 was selected as the flux, with $Fe_2(SO_4)_3$ and $CoSO_4$ as precursors. As expected, nanoplates of $CoFe_2O_4$ were obtained (Figure 2A−C). However, when Na_2MoO_4 was selected as the flux under otherwise identical conditions, octahedra of $CoFe_2O_4$ were obtained through melt crystallization via AMSS (Figure 2D−F). In contrast, polycrystalline micro-

DOI: 10.1021/acs.chemmater.5b00109
Chem. Mater. 2015, 27, 1863−1868

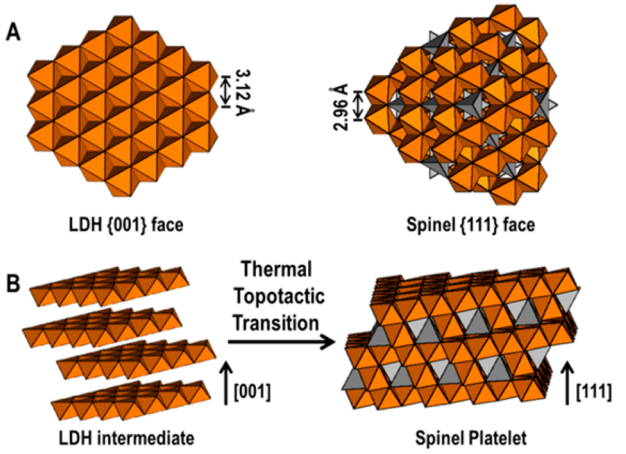

Figure 1. Schematics of (A) the LDH {001} face and spinel {111} face and (B) the conversion from a LDH intermediate to spinel product; (orange) octahedral and (gray) tetrahedral sites. Anion interlayers are omitted from the representation of the LDH. Inspired by ref 21.

spheres of $CoFe_2O_4$ along with an unindexed impurity were obtained as the USS product when no molten salt was incorporated (Figure S2, SI).

In the case of nanoplates, SEM of product without exposure to water indicates that several platelets are trapped within a spherical matrix, and each microsphere corresponds to one aerosol particle (Figure S3A, SI). XRD of the unwashed sample identifies Na_2SO_4 and Na_2CO_3 in addition to the $CoFe_2O_4$ product (Figure S3B, SI). EDS shows signals of sodium and sulfur, corresponding to components of the flux and precursors, which are facilely removed with collection and washing of the product with water (Figure S3C, SI), giving the plates shown in Figure 2A–C. These observations indicate that Na_2CO_3 spatially and temporally separates and confines the product particles without being incorporated. XRD of the washed sample is consistent with $CoFe_2O_4$ (Figure 3A). This

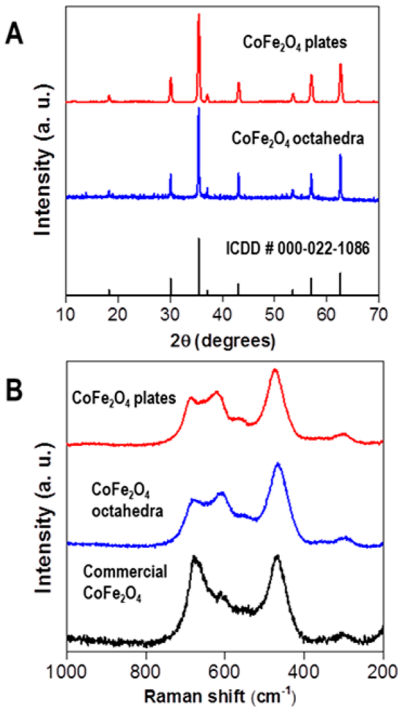

Figure 3. (A) XRD of the washed $CoFe_2O_4$ samples compared to reference card. (B) Raman spectra of $CoFe_2O_4$ nanoplates, $CoFe_2O_4$ octahedra, and a commercial $CoFe_2O_4$ sample.

assignment is further supported by Raman spectroscopy, where the peak positions of the nanoplate sample match those of commercial $CoFe_2O_4$ (Figure 3B) and literature

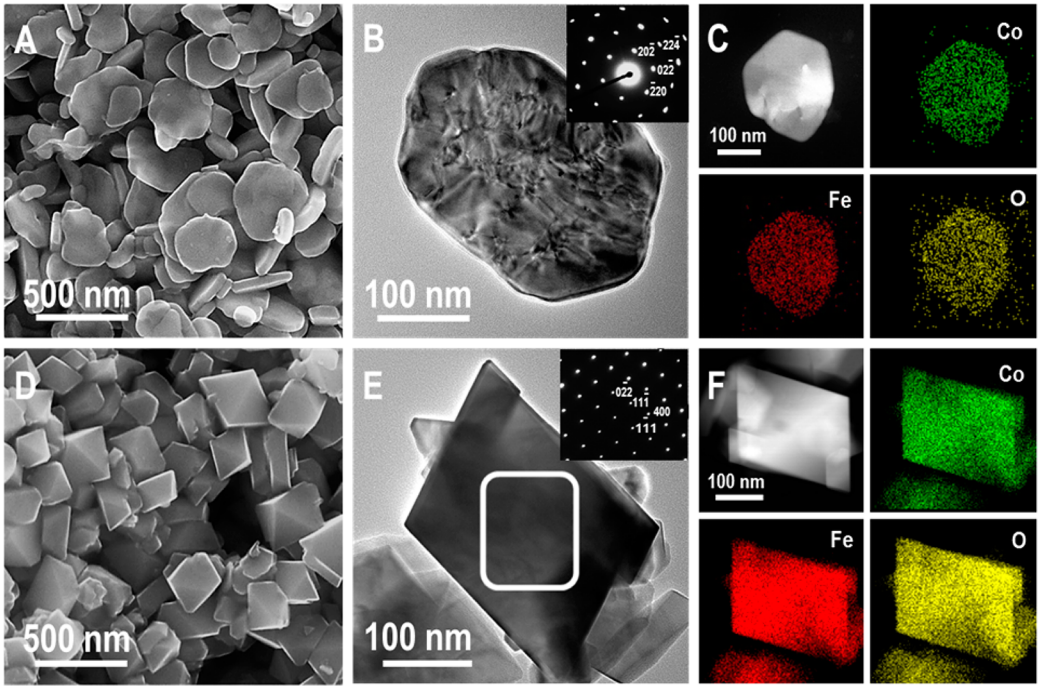

Figure 2. (A and D) SEM images, (B and E) TEM images (top insets, ED of a plate and selected area of a octahedron), (C and F) STEM images with elemental mapping of (A–C) a $CoFe_2O_4$ nanoplate and (D–F) a $CoFe_2O_4$ octahedron; (green) Co, (red) Fe, and (yellow) O.

DOI: 10.1021/acs.chemmater.5b00109
Chem. Mater. 2015, 27, 1863–1868

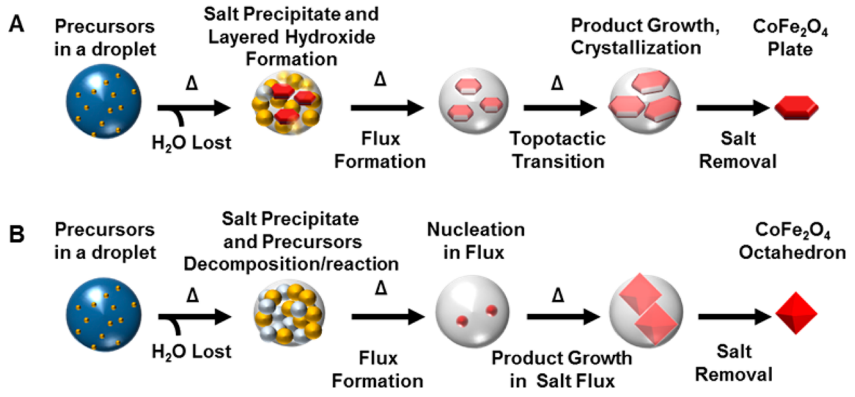

Figure 4. Schematics that account for (A) $CoFe_2O_4$ nanoplate formation via topotactic transition and (B) $CoFe_2O_4$ octahedra via direct melt crystallization.

reports.[24,25] The Raman peaks at 472 and 621 cm^{-1} correspond to Co^{2+} at octahedral and tetrahedral sites, respectively. $CoFe_2O_4$ usually adopts an inverse or a roughly inverse spinel structure, with Co^{2+} positioned at octahedral sites and half the Fe^{3+} in tetrahedral sites and the other half in octahedral sites. Compared to the commercial $CoFe_2O_4$, which has negligible Raman signal at 621 cm^{-1}, the $CoFe_2O_4$ nanoplate has an enhanced peak, indicating Co^{2+} at the tetrahedral sites. Migration of Co^{2+} from octahedral sites to tetrahedral sites is reported to influence the magnetization of the material.[25] Elemental mapping (Figure 2C) of a plate confirms that the elements are distributed throughout the structure, with a cobalt-to-iron ratio of 1:1.8. By TEM, the surface of the $CoFe_2O_4$ nanoplate seems uneven and to consist of several patches (Figure 2B). ED shows one set of spots consistent with single crystallinity, but closer review suggests slight lattice misorientation in the crystals as the spots are not perfectly circular (Figure 2B, inset). ED and analysis of lattice spacings in a HRTEM image indicate that the top and bottom of the nanoplates are bound by {111} facets (Figure S4, SI).

The role of a LDH intermediate in facilitating nanoplate formation was verified through a series of experiments. First, the temperature of the AMSS for $CoFe_2O_4$ nanoplates was lowered to 750, 800, and 850 °C. Because the topotactic transformation from the LDH to spinel phase requires heat, the LDH intermediate was anticipated to be the product at lower temperatures rather than the spinel product. Nanoplates were obtained at all temperatures, although sample quality decreased with decreasing temperature (Figure S5, SI). XRD patterns of the plates prepared at 750 and 800 °C indicate significant amorphous content with a diffraction envelope at low 2θ, which is similar in position to the (003) reflection of LDH phases[23,26] (Figure S5, SI). Second, CoFe-Na_2CO_3-80, which was prepared from the precursors used in AMSS of nanoplates but heated in solution at 80 °C rather than undergoing USS, was indexed to be the LDH $Co_{5.84}Fe_{2.16}(OH)_{16}(CO_3)_{1.08}$ by XRD (Figure S6, SI; referenced herein as CoFe-CO_3-LDH). CoFe-CO_3-LDH is a powder composed of plate-like particles which can be directly nebulized when dispersed in water (Figure S6, SI). When used as is, microspheres comprised of nanoplates are obtained (Figure S7, SI). With the addition of Na_2CO_3, the salt matrix inhibits subparticle agglomeration and $CoFe_2O_4$ nanoplates are obtained along with Fe_2O_3 impurities (Figure S8, SI). The $CoFe_2O_4$ phase was confirmed by XRD, Raman spectroscopy, and elemental mapping by STEM-EDS (Figure S8, SI).

However, EDS analysis of an individual plate indicates an Fe deficiency (Co/Fe = 1:1.3−1.4) on account of Fe_2O_3 formation and segregation. The phase separations might arise from different aerosol dynamics using LDH powders as the starting material for transition compared with the in situ generated LDH intermediate. Finally, other salts, including NaOH, Na_2MoO_4, NaCl, and Na_2SO_4, were used instead of Na_2CO_3 in USS under otherwise identical conditions. An LDH intermediate is only accessible in the case of NaOH due to its alkalinity. Mildly heating this precursor solution produces the platelet LDH precursor referred herein as CoFe-NaOH-80 (Figure S9, SI). As expected, $CoFe_2O_4$ plates were only generated when NaOH was incorporated into the USS (Figures S9 and S10, SI). A schematic accounting for spinel-phase nanoplates via AMSS is shown in Figure 4A, in which the in situ generated CoFe-LDH undergoes topotactic transformation to $CoFe_2O_4$ nanoplates in the Na_2CO_3 molten droplets.

Interestingly, when the slurry used for $CoFe_2O_4$ plate formation via AMSS was dried and then heated at 900 °C for comparison, a mixture of $NaFeO_2$ and $Fe_{0.88}O$ was confirmed by XRD (Figure S11, SI). Ill-defined particles were observed (Figure S11, SI). This finding highlights that crystals can grow differently in AMSS and MSS and may arise from the greater temperature gradient, shorter heating time and diffusion lengths, higher humidity, and absence of a possibly catalyzing surface during product formation via AMSS. These observations suggest that shape-controlled particles, which are unachievable by traditional MSS methods, can be produced in AMSS.

AMSS of Shape-Controlled $CoFe_2O_4$ Nanocrystals via Direct Melt Crystallization. Access to LDH intermediates need to be avoided if other nanocrystal shapes are to be prepared via AMSS. Na_2MoO_4 is an appropriate flux for the synthesis of shape-controlled nanocrystals of $CoFe_2O_4$ via crystallization from a molten droplet as Na_2MoO_4 is a good solvent to dissolve metal oxides.[27] Thus, with cooling, nucleation will proceed. Moreover, a LDH intermediate cannot be achieved from this solution formulation, where coprecipitation of the $CoSO_4$ and $Fe_2(SO_4)_3$ salts with $NaMoO_4$ followed by mild heating yielded a mixture of $CoMoO_4 \cdot 0.9H_2O$ and $Fe_2(MoO_4)_3 \cdot 8H_2O$ based on XRD, with micrometer-sized cylindrical aggregates observed by SEM imaging (Figure S12, SI).

Shown in Figure S13A (SI) is an SEM image of the AMSS product before washing with water. $CoFe_2O_4$ particles may be encased inside the molybdate-based matrix but are not visible.

DOI: 10.1021/acs.chemmater.5b00109
Chem. Mater. 2015, 27, 1863−1868

EDS analysis and XRD indicate both $CoFe_2O_4$ and Na_2MoO_4 (Figure S13, SI). The $CoFe_2O_4$ phase is released after washing with water, as confirmed by XRD and Raman spectroscopy (Figure 3). Similar to $CoFe_2O_4$ plates, $CoFe_2O_4$ octahedra have an increased Raman signal at 621 cm^{-1}, suggesting that Co^{2+} also resides at tetrahedral sites. The SEM image of the washed $CoFe_2O_4$ product revealed octahedral particles (Figure 2D). Elemental mapping of an individual particle by STEM-EDS indicates that the elements distribute evenly in the samples at a cobalt-to-iron ratio of 1:1.9 (Figure 2F). TEM and ED from the selected region of the octahedron indicate that the particles are single-crystalline (Figure 2E).

$CoMoO_4$ and $Fe_2(MoO_4)_3$, likely form when the precursors of AMSS $CoFe_2O_4$ octahedra, are mildly heated in the beginning of the synthesis (Figure S12, SI). These intermediates can decompose to Fe_2O_3, CoO, and MoO_3 at higher temperature. TGA and DSC analysis were used to study the thermal behavior of the precursors (Figure S14, SI). The endothermic peaks in the DSC curve together with the continuous mass loss measured by TGA below 200 °C arise from water loss. The small features at ∼260, 285, and 330 °C with correspondingly negligible mass loss can be attributed to phase transitions of the precursors. The sharp endothermic peak at ∼480 °C corresponds to melting. These assignments are supported by the thermal analyses of a $Fe_2(SO_4)_3$ and Na_2MoO_4 mixture and a $CoSO_4$ and Na_2MoO_4 mixture, respectively (Figure S14, SI). Thus, we hypothesize that $CoFe_2O_4$ nucleates after saturation and grows directly into octahedra from the Na_2MoO_4 flux, which is consistent with the fcc crystal habit of spinel. A schematic accounting for octahedral particle formation is shown in Figure 4B. Interestingly, when the precursor solution used to prepare $CoFe_2O_4$ octahedra is dried and used in a traditional MSS, the product consists of particles with varied morphology, including octahedra (Figure S15, SI). The XRD pattern indicates the $CoFe_2O_4$ phase and impurity from the Pt pan, again suggesting that the structures achieved by AMSS are often different from that of traditional MSS.

CONCLUSIONS

As demonstrated with $CoFe_2O_4$ as a model system, solution formulation can direct crystal growth in AMSS to achieve nanocrystals of different shapes. Here, $CoFe_2O_4$ nanoplates and octahedra are selectively achieved through the selection of flux. In the case of $CoFe_2O_4$ nanoplate formation, flux selection facilitates and stabilizes LDH intermediate platelets, which undergo topotactic conversion to the spinel phase with preservation of crystal shape. However, the LDH intermediate can be bypassed through selection of Na_2MoO_4 as the flux. In this system, $CoFe_2O_4$ octahedra are formed through crystallization from the molten salt droplets, adopting an equilibrium crystal habit. Thus, selection of the salt component in AMSS provides a pathway to nanocrystals with different shapes, where either the conditions of supersaturation are directly modulated by the technique or precursor chemistry provides a new pathway to product. Moreover, given the variety of molten salts[12,27−30] and systems capable of topotactic transformations,[21,31−33] AMSS represents a promising approach toward shape- or phase-controlled nanocrystals which are not readily achieved via other methods.

ASSOCIATED CONTENT

Supporting Information

Schematic of the USS setup and additional characterization of products and results from control studies. This material is available free of charge via the Internet at http://pubs.acs.org.

AUTHOR INFORMATION

Corresponding Author

*E-mail: sskrabal@indiana.edu.

Present Address

†Electrical and Computer Engineering Department, Rice University, 6100 Main St., Houston, Texas 77005. E-mail: cjd7@rice.edu

Author Contributions

Elemental mapping by STEM-EDS and ED conducted by C.J.D. and R.G.W. All other experiments by J.F. Manuscript preparation by J.F. and S.E.S.

Notes

The authors declare no competing financial interest.

ACKNOWLEDGMENTS

We acknowledge financial support from Indiana University (start-up) and NSF CAREER DMR-0955028. S. Skrabalak is a Cottrell Scholar (Research Corporation for Science Advancement, RCSA), Sloan Research Fellow, and Camille Dreyfus Teacher-Scholar Awardee. Access to the powder diffractometer was provided by NSF CRIF CHE-1048613. SEM, EDS, and TGA were performed at Indiana University's Nanoscience Center. We also thank Dr. Maren Pink of the Indiana University Molecular Structure Center and Dr. David Morgan of the Indiana University Nanoscience Center for their help on JEOL JEM 3200FS TEM.

REFERENCES

(1) Li, Y.; Takata, T.; Cha, D.; Takanabe, K.; Minegishi, T.; Kubota, J.; Domen, K. *Adv. Mater.* **2013**, *25*, 125.

(2) Sun, M.; Xiong, S.; Wu, X.; He, C.; Li, T.; Chu, P. K. *Adv. Mater.* **2013**, *25*, 2035.

(3) Wang, L.; Ge, J.; Wang, A.; Deng, M.; Wang, X.; Bai, S.; Li, R.; Jiang, J.; Zhang, Q.; Luo, Y.; Xiong, Y. *Angew. Chem. Int. Ed.* **2014**, *53*, 5107.

(4) Xie, J.; Zhang, J.; Li, S.; Grote, F.; Zhang, X.; Zhang, H.; Wang, R.; Lei, Y.; Pan, B.; Xie, Y. *J. Am. Chem. Soc.* **2013**, *135*, 17881.

(5) Bang, J. H.; Helmich, R. J.; Suslick, K. S. *Adv. Mater.* **2008**, *20*, 2599.

(6) Jung, K. Y.; Lee, H. W.; Kang, Y. C.; Park, S. B.; Yang, Y. S. *Chem. Mater.* **2005**, *17*, 2729.

(7) Okuyama, K.; Lenggoro, I. W. *Chem. Eng. Sci.* **2003**, *58*, 537.

(8) Gurav, A.; Kodas, T.; Pluym, T.; Xiong, Y. *Aerosol Sci. Technol.* **1993**, *19*, 411.

(9) Mann, A. K. P.; Skrabalak, S. E. *Chem. Mater.* **2011**, *23*, 1017.

(10) Mann, A. K. P.; Wicker, S.; Skrabalak, S. E. *Adv. Mater.* **2012**, *25*, 1549.

(11) Mann, A. K. P.; Fu, J.; DeSantis, C. J.; Skrabalak, S. E. *Chem. Mater.* **2013**, *25*, 1549.

(12) Kimura, T. *Molten Salt Synthesis of Ceramic Powders*. InTech: Rijeka, Croatia2011.

(13) Peddis, D.; Cannas, C.; Musinu, A.; Ardu, A.; Orrù, F.; Fiorani, D.; Laureti, S.; Rinaldi, D.; Muscas, G.; Concas, G.; Piccaluga, G. *Chem. Mater.* **2013**, *25*, 2005.

(14) Manova, E.; Kunev, B.; Paneva, D.; Mitov, I.; Petrov, L.; Estournès, C.; D'Orléan, C.; Rehspringer, J.-L.; Kurmoo, M. *Chem. Mater.* **2004**, *16*, 5689.

DOI: 10.1021/acs.chemmater.5b00109
Chem. Mater. 2015, 27, 1863−1868

(15) Huo, R.; Jiang, W. J.; Xu, S.; Zhang, F.; Hu, J. S. *Nanoscale* **2014**, *6*, 203.
(16) Xiong, P.; Chen, Q.; He, M.; Sun, X.; Wang, X. *J. Mater. Chem.* **2012**, *22*, 17485.
(17) Uzunova, E.; Klissurski, D.; Mitov, I.; Stefanov, P. *Chem. Mater.* **1993**, *5*, 576.
(18) Ji, G.; Lin, X.; Sun, Y.; Trimizi, S. A. A.; Su, H.; Du, Y. *CrystEngComm* **2011**, *13*, 6451.
(19) Lee, J.-G.; Park, J. Y.; Oh, Y.-J.; Kim, C. S. *J. Appl. Phys.* **1998**, *84*, 2801.
(20) Amethyst Galleries' Mineral Gallery, http://www.galleries.com/spinel_group (accessed Oct 20, 2014).
(21) Kobayashi, Y.; Ke, X.; Hata, H.; Schiffer, P.; Mallouk, T. *Chem. Mater.* **2008**, *20*, 2374.
(22) Li, M.; Yin, Y. X.; Li, C.; Zhang, F.; Wan, L. J.; Xu, S.; Evans, D. G. *Chem. Commun.* **2012**, *48*, 410.
(23) Zhao, X.; Zhang, Y.; Xu, S.; Lei, X.; Zhang, F. *J. Phys. Chem. C* **2012**, *116*, 5288.
(24) Naik, S. R.; Salker, A. V. *J. Mater. Chem.* **2012**, *22*, 2740.
(25) Sharma, D.; Khare, N. *Appl. Phys. Lett.* **2014**, *105*, 032404.
(26) Shao, M.; Wei, M.; Evans, D. G.; Duan, X. *Chem. Commun.* **2011**, *47*, 3171.
(27) Bugaris, D. E.; zur Loye, H.-C. *Angew. Chem., Int. Ed.* **2012**, *51*, 3780.
(28) Akdogan, E.; Brennan, R.; Allahverdi, M.; Safari, A. *J. Electroceram.* **2006**, *16*, 159.
(29) Zhou, H.; Mao, Y.; Wong, S. S. *Chem. Mater.* **2007**, *19*, 5238.
(30) Yoon, K. H.; Cho, Y. S.; Kang, D. H. *J. Mater. Sci.* **1998**, *33*, 2977.
(31) Kong, X.; Hu, D.; Wen, P.; Ishii, T.; Tanaka, Y.; Feng, Q. *Dalton Trans.* **2013**, *42*, 7699.
(32) Guo, C. F.; Cao, S.; Zhang, J.; Tang, H.; Guo, S.; Tian, Y.; Liu, Q. *J. Am. Chem. Soc.* **2011**, *133*, 8211.
(33) Sun, Y.; Li, C.; Zheng, W. *Cryst. Growth Des.* **2010**, *10*, 262.

DOI: 10.1021/acs.chemmater.5b00109
Chem. Mater. 2015, 27, 1863−1868